November 1975
C003237-52

Numerical Studies of Nonlinear Evolution of Kink Modes in Tokamaks*

M. N. Rosenbluth†, D. A. Monticello††, H. Strauss†††
Institute for Advanced Study, Princeton, New Jersey 08540

and

R. B. White
Princeton University, Plasma Physics Laboratory, Princeton, New Jersey 08540

A set of numerical techniques for investigating the full nonlinear unstable behavior of low-β kink modes of given helical symmetry in tokamaks is presented. Uniform current density plasmas display complicated deformations including the formation of large vacuum bubbles provided that the safety factor q is sufficiently close to integral. Fairly large $m = 1$ deformations, but not bubble formation, persist for a plasma with a parabolic current density profile (and hence shear). Deformations for $m \geq 2$ are, however, greatly suppressed.

† Also at the Plasma Physics Laboratory, Princeton University

†† Present address, Plasma Physics Laboratory, Princeton University.

††† Present address, University of Texas at Austin, Austin Texas 78712

* This work was supported by U.S. Energy Research and Development Administration Contract Nos. AT(11-1)-3232 and E(11-1)-3073. Thanks are due to P. H. Rutherford, D. Potter, J. M. Greene, J. L. Johnson, R. C. Grimm, M. Chance, C. Liu, and B. Waddell for helpful discussions.

I. INTRODUCTION

It has been suggested by Kadomtsev[1] that the kink mode plays an instrumental role in the disruptive instability seen in tokomaks. The imagined mechanism is that the nonlinear kink mode development leads to highly distorted shapes with the vacuum on the inside and plasma on the outside, the so-called bubble state. Rutherford, Furth, and Rosenbluth, in an earlier work[2] pointed out that for a constant current profile the plasma does not possess nearby bifurcated states for plasma radius greater than $r_c = 0.7\, r_{wall}$, and thus the final state might be highly distorted.

The expected large distortions of the plasma led us to treat the problem by numerical methods. A numerical treatment of the nonlinear kink mode in tokamaks in a straightforward way is difficult however because of the various time scales involved (Alfven waves and sound waves, and relatively slow kinks) and because of the free boundary between plasma and vacuum. In Sec. II, we present a reduced set of equations which in the tokamak ordering describe the full nonlinear development of the kink mode. The use of this reduced set of equations in a numerical scheme avoids most of the above mentioned difficulties. The equilibrium state and the linear theory of the kink modes are reviewed in Sec. III and Sec. IV, respectively. The results of numerically integrating the reduced equations are presented for two distinct cases. The first case, described in Sec. V, is that of constant current, no shear, with the helical pitch of

DISTRIBUTION OF THIS DOCUMENT IS UNLIMITED

DISCLAIMER

the perturbation exactly matching the pitch of the equilibrium field in the plasma. By adding surface current, which is equivalent to changing the safety factor q at the plasma surface, the equilibrium may be made linearly stable or unstable. In this case, the conjecture of Kadomtsev is verified. The obtained bubble states are however not the nonlinear result of the case studied by Rutherford, Furth and Rosenbluth. As a function of the safety factor q the growth rate for the linear kink mode has two marginal stable points. The case they examined was a mode near the marginal stable point where only one mode is unstable. We find that in this region, even though the distortion is greater than a third order bifurcation theory could hope to follow, it is mild compared to the true bubble states. These are found for q in the vicinity of the marginal stable point where all modes with the same ratio of m/n are unstable.

The second case, described in Sec VI, is that of a non-constant current profile, and hence with magnetic shear. As might be expected, the stabilizing effect of shear is very strong. In fact, we find that for a parabolic current profile ($q(0) = 1/2\, q(r_s)$) and $m \geq 2$ the distortions are very mild and not at all bubble-like. However, appreciable distortions without bubble formation are still observed particularly for $m = 1$ modes. Nonlinear behavior with parabolic current profiles for $m \geq 2$ is generally mild enough to conclude that <u>ideal</u> MHD kink instabilities with $q > 1$ do not represent a threat to tokomak confinement.

II. THE REDUCED SET OF EQUATIONS

The energy reservoir for free boundary kinks is very large and the toroidal case is adequately treated by the cylindrical approximation. Hence, we model the tokomak by a cylinder of length $L = 2\pi R$, R the major radius of the plasma.

We also restrict ourselves to following the nonlinear development of perturbations of a fixed helical symmetry. This, together with the fact that the walls and equilibrium are cylindrical, implies that all quantities are functions of τ, r, and t only, where $\tau = m\theta + kz$ and $k = n/R$. Here, m and n are the mode numbers of the original perturbation, which has the form $f(r)\cdot\exp(i\,[m\theta + kz])$.

Helical symmetry has the obvious advantage of reducing the three dimensional numerical calculation to a two dimensional one ($\frac{\partial}{\partial z} = \frac{k}{m}\,\frac{\partial}{\partial \theta}$). In addition, this symmetry, together with $\nabla\cdot B = 0$ implies that B_θ, B_r, and B_z may be related to a scalar ψ by

$$B_r = \frac{1}{r}\frac{\partial \psi}{\partial \theta}\,, \quad B_\theta = -\frac{\partial \psi}{\partial r} - \frac{kr}{m}\,B_z \qquad (1)$$

or

$$\vec{B} = \vec{\nabla}\psi \times \hat{z} - \frac{kr}{m}\,B_z\hat{\theta} + B_z\hat{z}\,. \qquad (2)$$

The function ψ is a flux function, i.e., $(B \cdot \nabla)\psi = 0$. It is in fact proportional to flux through a helical ribbon defined by the magnetic axis and a helix of constant r , hence the name helical flux. In addition, ψ is related to the magnetic vector potential by

$$\psi = A_z - \frac{kr}{m} A_\theta \tag{3}$$

and the dynamical behavior

$$\frac{D\psi}{Dt} = 0 \tag{4}$$

then follows from Faraday's law and the assumption of infinite conductivity. (Here $\frac{D}{Dt}$ is the convective time derivative.) Equation (4) can also be derived by using the particle Hamiltonian, and is simply the statement that the magnetic field is frozen in the plasma. It is convenient to use ψ in a numerical scheme to guarantee this property. The ideal MHD equations,

$$\begin{aligned} \nabla \cdot B &= 0 & \nabla \times B &= J \\ E &= -v \times B & \nabla \times E &= -\frac{\partial B}{\partial t} \\ \rho \frac{Dv}{Dt} &= J \times B - \nabla P & \frac{D\rho}{Dt} &= -\rho \nabla \cdot v \\ \frac{DP}{Dt} &= -\gamma P \nabla \cdot v \end{aligned} \tag{5}$$

can be further simplified by using the large aspect ratio of tokomaks and expanding in $\varepsilon = \frac{kr}{m} = (\frac{n}{m})(\frac{r}{R}) << 1$.

From the observed $\beta_\theta \sim \frac{P}{B_\theta^2} \sim 1$ and $q \sim \frac{r_s B_z}{R B_\theta} \sim 1$, we find the following consistent ordering scheme for kink modes:

$$\begin{aligned} &O(1) : B_{z0} , \rho , \nabla_\perp , \\ &O(\varepsilon) : B_\theta , B_r , J_z , V_\perp , \frac{\partial}{\partial t} , \frac{\partial}{\partial z} \\ &O(\varepsilon^2): \tilde{B}_z , P , J_\perp , V_z \\ &O(\varepsilon^3): \nabla_\perp \cdot V_\perp \end{aligned} \tag{6}$$

where $\tilde{B}_z$ is the perturbation field, $B_z = B_{z0} + \tilde{B}_z$. With this ordering, we find that the equation of motion $\rho \frac{DV}{Dt} = -\nabla P + J \times B$ can be reduced, upon substituting $J = \nabla \times B$ and using Eq. (2) for $\vec{B}$, and keeping only lowest order terms in kr to

$$\rho \frac{DV_\perp}{Dt} + \nabla_\perp \{P + \frac{B^2}{2} - \frac{(\nabla_\perp \psi)^2}{2} + \frac{2kB_z\psi}{m} + \frac{1}{2}(\frac{kB_z r}{m})^2 \} + \nabla_\perp \psi \nabla_\perp^2 \psi = 0 \tag{7}$$

Similarly, we find, to complete the set of reduced equations

$$\frac{D\psi}{Dt} = 0 \tag{8}$$

$$J_z = -\nabla_\perp^2\psi - \frac{2k}{m} B_{z0} \tag{9}$$

$$\nabla_\perp \cdot V_\perp = 0 \tag{10}$$

where all quantities are now functions of r, θ, t only and the three dimensional result is to be obtained by the helical extension $\theta \to \theta + \frac{k}{m} z$.

In the vacuum the components of $\nabla \times B = 0$ give

$$\nabla_\perp^2\psi = -\frac{2kB_z}{m} \tag{11}$$

$$\frac{B^2}{2} = -\frac{1}{2}\left(\frac{kB_z r}{m}\right)^2 + \frac{(\nabla_\perp\psi)^2}{2} + \text{const.} \tag{12}$$

We eliminate the unknown $\tilde{B}_z$ from Eq. (7) in the standard manner by taking its curl. The equations are now complete since the divergence of $V_\perp$ is also known from Eq. (10), expressing incompressibility in the r-θ plane. This incompressibility is also important from the numerical point of view since the fastest wave now possible is the incompressible

Alfven wave ($v_{phase} \sim \varepsilon$) and not the fast magnetosonic wave which is one order faster.

Incompressibility can further be used to reduce the number of variables by introducing a scalar potential A to represent $\vec{v}_\perp$. We treat the large surface current as infinitesimally thin and derive a boundary condition for $\frac{\partial A}{\partial n}$ by using the pressure balance across it:

$$P + \frac{B^2}{2}\Big|_p = \frac{B^2}{2}\Big|_v \tag{13}$$

and Eq. (12) for B_v^2. (See Appendix A.) We then make the equations dimensionless through the transformations:

$$\bar{t} = \frac{t}{\sqrt{\rho}\, m/(B_z k)}, \quad \bar{A} = \frac{A}{(kr_w^2 B_z/m\sqrt{\rho})}$$

$$\bar{r} = \frac{r}{r_w}, \quad \bar{\psi} = \frac{\psi}{(kr_w^2 B_z/m)} \tag{14}$$

The resulting set of reduced equations which describe the behavior of the kink modes in a tokamak is then

Plasma:

$$\frac{D\psi}{Dt} = 0 \tag{15}$$

$$\frac{D\nabla_\perp^2 A}{Dt} = -\nabla_\perp\psi \times \nabla_\perp(\nabla_\perp^2\psi) \tag{16}$$

$$\vec{v}_\perp = \frac{D\vec{r}}{Dt} = -\hat{z} \times \nabla_\perp A \tag{17}$$

$$\frac{D\frac{\partial A}{\partial n}}{Dt} = \frac{1}{2}\hat{p}\cdot\vec{\nabla}_\perp\{(\nabla\psi)_v^2 - (\nabla\psi)_p^2\} - (v_\perp\cdot\hat{n})\hat{n}\cdot(\hat{p}\cdot\vec{\nabla})\vec{v}_\perp \tag{18}$$

where $\hat{p}$ is the counterclockwise parallel to the plasma surface.

Vacuum:

$$\nabla_\perp^2\psi = -2 \tag{19}$$

Boundary Conditions:

$$\psi_{p-v} = 0 \tag{20}$$

$$\psi(r=1) = \psi_w(\text{wall}) \tag{21}$$

The usual condition at the plasma surface (necessary to avoid infinite forces)

$$\vec{B}\cdot\hat{n}_H = 0 \tag{22}$$

implies that ψ is uniform over the surface of the plasma. (Here, $\hat{n}_H$ is the normal to the helically distorted surface, and does not necessarily lie in the r,θ plane. The symbols $\hat{n}$ and $\hat{p}$ will refer to normals and parallels to the intersection of the plasma surface with the r,θ plane.) This condition, together with $\frac{D\psi}{Dt} = 0$, yields the boundary condition Eq. (20). Similarly, the boundary condition Eq. (21) follows from $\vec{B}\cdot\hat{n} = 0$ at the perfectly conducting wall.

It is now possible to carry out the integration in time of Eqs. (15-21) imposing as constraint either $E_z(\text{wall}) = -\frac{\partial\psi}{\partial t} = 0$, or I = constant, where E_z is the z component of the electric field at the conducting surface and I is the total plasma current. Results quoted below are for the case $E_z = 0$.

The procedure for numerically integrating the equations is now apparent. ψ, A, $\vec{r}$ are specified at time, t. $(\nabla\psi)_v^2$ is found from solving Eq. (19). Equations (16, 18) give $\nabla^2 A$ and $\frac{\partial A}{\partial n}$ at time, $t+\Delta t$. Poissons' equation is then solved to find A at time, $t+\Delta t$, and Eqs. (17, 15) are used to advance $\vec{r}$ and ψ.

As might be expected, these equations possess an energy integral;

$$\int_{\text{plasma}} \left(\frac{v^2}{2} + \frac{(\nabla\psi)^2}{2}\right) r dr d\theta \; - \int_{\text{vacuum}} \frac{(\nabla\psi)^2}{2} r dr d\theta \; + \; 2\pi\psi_w b = \text{const.} \qquad (23)$$

where $b = -I/2\pi$. This integral, derived in Appendix B, serves as a starting point for an analytic calculation of the energy of bubble states discussed in Sec. V C.

III. EQUILIBRIUM

We consider only the cylindrical equilibrium shown in Fig. 1. The equilibrium is completely specified by choosing the plasma radius a , $J_z(r)$ for $r \leq a$, and J_z^* , the skin current. (The pressure and B_z profile are unimportant since they do not enter into Eqs. (15-18).) It is more convenient however, to use a dimensionless quantity such as the safety factor $q(r)$

$$q(r) \; = \; - \frac{rB_z}{RB_\theta} \qquad (24)$$

which in the scaled variables given by Eq. (14) becomes

$$q(r) \; = \; - \left(\frac{m}{n}\right)\left(\frac{r}{B_\theta}\right) \qquad (25)$$

The equilibrium is then specified by a and $q(r)$, $r \leq a$ and the safety factor q just outside the plasma vacuum interface. The equilibrium ψ_0 is found by solving the differential equation

$$\psi_0' \; = \; \left(\frac{m}{n\,q(r)} - 1\right) r \qquad (26)$$

with the boundary condition that $\psi(a) = 0$. In the vacuum ψ_0 is found by solving Eq. (19) with boundary conditions given by Eqs. (20, 21) giving

$$\psi_{0V}(r) \; = \; \frac{(1 - r^2)}{2} + b_1 \ell n\, r + \psi_w \qquad (27)$$

where $b_1 = ((a^2-1)/2 - \psi_w)/\ell n a$ and $\psi_w = (a^2-1)/2 - \frac{m}{n}(a^2 \ell n a)/q$.

Note that ψ_0 , as determined by Eqs. (26, 27) is a function of the ratio m/n , i.e., its form depends on the mode numbers of the perturbation to be considered.

The unperturbed current and magnetic field can now be obtained through Eq. (9), which becomes $J_z = -\nabla_\perp^2 \psi - 2$ when expressed in terms of the transformed variables given by Eq. (14) . The expression for the skin current is

$$J_z^* \; = \; \frac{m}{n}\, a \left(\frac{1}{q(a)} \; - \frac{1}{q}\right) \; . \qquad (28)$$

IV. LINEAR THEORY

A kink mode solution of the linearized form of Eqs. (15-21) can be obtained analytically only for special cases such as constant current. The results, which we quote here, are well known.[3] The modes grow as $e^{\gamma t}$ with

$$\gamma^2 = m\Delta\,((1-mh)\Delta + 2) - 4\,b_2^2(m-1)m \tag{29}$$

where $\Delta = \frac{m}{nq} - 1$, $h = \frac{1+a^{2m}}{1-a^{2m}}$, and $b_2 = (\frac{m}{nq(a)}-1)\frac{1}{2}$.

In this case, $\psi_0 = b_2(r^2 - a^2)$ and $\tilde{A} \sim r^m\cos(m\theta)$, i.e., $\tilde{v}_\perp$ is curl-free and $\nabla^2\tilde{A} = 0$. In the ordering given by Eq. (6) only the kink modes are unstable to lowest order. The internal kink and Mercier modes are at most neutral stable. For the case of non-constant current the growth rates were found using a numerical scheme[4] to integrate the resulting ordinary differential equation.

V. CASE I; $\psi \equiv 0$ and $\nabla \times V_\perp = 0$ in the Plasma

A. Simplification of the Reduced Equations

From the point of view of numerical analysis, the study of Eqs. (15-21) breaks up into two distinct cases. We note from Eq. (16) that if $\nabla \times V_\perp = 0$ initially, it will always remain so, provided ψ is identically zero within the plasma.

In this case, we can write $\vec{v} = \nabla\phi$ and Eq. (16) becomes

$$\nabla_\perp^2\phi = 0 \tag{30}$$

and Eq. (17) is reduced to

$$\frac{d\vec{r}_s}{dt} = \nabla\phi$$

since in this case, the plasma interior being uniform, the problem is reduced to following the motion of the plasma vacuum interface. The boundary condition Eq. (18) becomes

$$\left.\frac{D\phi}{Dt}\right|_{p-v} = -\frac{1}{2}\left[\,(\nabla_\perp\psi)_v^2 - (\nabla_\perp\phi)_p^2\,\right] \tag{32}$$

The procedure for advancing the solution forward in time is as follows: ϕ, $\frac{\partial\phi}{\partial n}$ are given at time t on the boundary $\vec{r}_s$. Equation (19) can be solved to give $(\nabla_\perp\psi)_v^2$. Now $\vec{r}_s$ and ϕ on the boundary can be advanced with Eqs. (31, 32). Given the time advanced surface, $\nabla^2\phi = 0$ with ϕ known on the boundary gives $\frac{\partial\phi}{\partial n}$ on the boundary at the new time. The numerical simplicity of this case is now obvious. One needs only a one-dimensional grid on the surface of the plasma. As described in Sec. V E, Laplace's equation can be solved for $\frac{\partial\phi}{\partial n}$ without the use of an internal grid.

B. Linear Theory

The case of ψ equal to zero in the plasma is an interesting case also because $q(r) = m/n$ maximizes the growth rate, as can be seen from Eq. (29). The growth rate is shown in Fig. 2. We note here that if the initial perturbation has mode numbers n, m, only modes with the same ratio of n/m will be produced through the nonlinear coupling. Note for example that if $q = 0.45$, an initial perturbation with mode numbers $n = 1$, $m = 1$ couples to the mode $n = 2$, $m = 2$, which is unstable, and to $n = 3$, $m = 3$, which is stable, etc. We refer to the point $nq/m = 1$, where all modes with the same value of n/m are neutral stable, as the right hand neutral stable point.

C. Nonlinear Stable Equilibrium, Bubbles

As first pointed out by Kadomtsev,[1] from the expression for the energy, it is easily seen that states consisting of a vacuum bubble surrounded by plasma (for accessibility, the bubble must be imagined to be connected to the outside via a thin slit allowing flux penetration) may be of lower energy than the equilibrium configuration. Consider a centrally located vacuum bubble of radius r_b, the plasma, thus, extending from r_b to $r_1 = (a^2 + r_b^2)^{1/2}$, where a is the equilibrium plasma radius. Inside the bubble we have $\psi = -r^2/2$ const and outside $\psi = (1 - r^2)/2 + b' \ell n\, r + \psi_w$ where $b' = [-\psi_w - \frac{(1 - r_1^2)}{2}]/\ell n r_1$. For the case in which ψ_w is a constant of the motion (see Appendix B), we use Eq. (23) to find the energy of the bubble state to be given by

$$E_b = \pi r_1^2 a^2/2 - \pi [(1 - r_1^2)/2 + \psi_w]^2/\ell n\, r_1 + \text{const} \qquad (33)$$

where the constant is independent of ψ_w and r_1.

Figure 3 shows the bubble state energy as a function of r_1 for various values of ψ_w (or equivalently q) for the case $a = 0.5$. Flux trapping ensures that the energy approaches infinity as $r_1 \to 1.0$ except for the particular case $\psi_w = 0$. For a wide range of values of mq/n, the bubble state is energetically favored. In Fig. 2, this range of values is shown along with the growth rates for the linear modes. Note that the bubble region extends beyond the region of linear instability. Although this analytic calculation indeed shows the existence of bubble states with lower energy than the initial state, it is not clear that these states are accessible from the initial configuration, or that there is not a large potential barrier which would effectively prevent their occurrence. Note that the curve in Fig. 3 does not represent the energy following a phase path initiating from a kink mode perturbation, and thus does not indicate the result of such a perturbation. The

actual phase space of surface distortions is of course extremely large, and only a full numerical investigation of the actual evolution of the plasma can decide the question of the accessibility of the bubble states.

An analytic calculation can also be made near the left hand neutral stable point where $\psi_w > 0$. A perturbation expansion of the equations for an $m = 1$ displacement in the vicinity of the left hand neutral stable point (see Fig. 2) leads to an equation of motion

$$\delta\ddot{r} = -\omega^2 \delta r + C(a)\, \delta r^3 \quad . \tag{34}$$

We find that the term $C(a)$ is stabilizing for $a < 0.65$; otherwise no nearby equilibrium exists. (A similar result was found in a calculation,[2] in which the skin current was zero.) By introducing a damping term $(-\nu\dot{\phi})$ into Eq. (32), the final asymptotic state can be found numerically. The nearby states found in this manner had displacements agreeing within a few percent with the value $\delta r = [\omega^2/C(a)]^{1/2}$ given by Eq. (34) for $a < 0.65$. With $a > 0.65$ the displacements are more distorted than a third order theory could be expected to describe, but quite mild compared to bubbles.

Equation (34) was also used to investigate the threshold for finite amplitude displacements to the left of the neutral stable point when $C(a)$ is destabilizing but the mode is linearly stable. In this case the magnitude of the necessary threshold perturbations can be calculated and were found to be in agreement with the numerical results.

D. Results of the Numerical Integration

In Fig. 4 is shown the time evolution of the plasma-vacuum boundary following an $m = 1$ perturbation. We have chosen a case which exhibits the formation of a bubble, $a = 0.7$, $\frac{nq}{m} = 1.0$. In spite of the rather violent distortions, the plasma behaves quite elastically, cases with less violent bubble formation having been run through several nonlinear oscillation periods. (Here we refer simply to the maximum inward extension of the concave part of the plasma, periodic motion in the sense of the plasma returning to its original configuration is not observed.)

Most of the numerical runs were used to find minimum energy states, the purpose here being twofold. First, this reveals the state to which the plasma would proceed in the presence of energy loss mechanisms. Secondly, they give a good measure of the maximum distortion that could be expected from a time history of the undamped plasma.

Introducing a damping term $-\nu\dot{\phi}$ into Eq. (32) allows one to find final asymptotic minimal energy states numerically. Near the left-hand neutral stable point (Fig. 2) where a small number of modes are linearly unstable, the plasma exhibits a

shallow deformation which gradually deepens as $\psi_w \to 0$. However, the quantity $(\partial\psi/\partial n)$ evaluated on the surface (which determines the skin current since $\psi \equiv 0$ in the plasma interior), always points outward and has a constant magnitude everywhere on the surface, a condition which can be seen necessary for equilibrium from Eq. (32). For $\psi_w < 0$, however, $(\partial\psi/\partial n)$ becomes discontinuous, the plasma forming sharp horns at the points of discontinuity which tend to close off the resulting vacuum bubble. For numerical reasons a complete bubble is not seen, but as the number of points is increased the horns approach each other more closely, evidently asymptoting to a completely enclosed bubble, whose size agrees with the energetic minimum predicted analytically by Eq. (33). In Figs. 5 and 6, the range of final states obtained is shown for $a = 0.8$, and $a = 0.5$. Figure 7 shows final states obtained for $m = 2, 3$, $a = 0.7$, with $nq/m = 1.0$.

As can be seen from Figs. (5) and (6), the bubble states (characterized by the formation of sharp horns which attempt to pinch off the bubble) are found to be the true energetic minima only for $\psi_w < 0$. The predicted bubble radius and $\frac{\partial \psi}{\partial n}$ agree very closely with the numerical results in this case. (Note that for a true equilibrium to result the sharp horns must proceed to the point where the inner and outer plasma surfaces become tangent. The energy of the final state,

however, is independent of the position of the inner bubble within the plasma.) For $\psi_w > 0$ the minimum energy states found numerically are strongly concave, but are not bubble states.

E. Numerical Analysis of the Nonlinear Behavior

Various numerical methods have been tried--considerable difficulty arising because of the rather extreme distortions of the surface which occur and the impossibility of using simple Fourier representations. A satisfactory scheme seems to be the following: The surface is represented by a set of mass points moving with velocity $\nabla\phi$. The necessary potentials, ϕ in the plasma and ψ in the vacuum, are determined by using Gauss' theorem to relate the normal derivatives of ϕ and ψ to their values on the surface, and mass points may be slid along the surface with proper interpolation in order to retain an adequate representation. The basic time step then consists of matrix inversions of the integral equation along the surface. Linear growth rates and oscillation periods are determined with accuracies of 10^{-3} with 20 particles on the surface. Let r_s be a point on the plasma surface and $\vec{n}$ the outward normal (see Fig. 8a). Using Gauss' theorem, we find for the velocity potential ϕ,

$$\phi(r_s) = \frac{1}{\pi} \int_c \{ \phi(r) \frac{\partial}{\partial n} \ell n \, | \vec{r} - \vec{r}_s | - \ell n | \vec{r} - \vec{r}_s | \, \frac{\partial \phi}{\partial n} \} \, ds \qquad (35)$$

where the contour c is the plasma boundary and the integral is a principle value integral at $r = r_s$.

The flux function ψ can be written $\psi = -1/2(r^2-1) + \psi_w + A(\vec{r})$ with $A(\vec{r})$ harmonic in the vacuum, $A(\vec{r}) = 0$, $|\vec{r}| = 1$, and the integration contour becomes that shown in Fig. 8b . The vector $\vec{n}'$ is in this case the outward normal to the vacuum region. In this case, we have

$$A(\vec{r}_s) = \frac{1}{\pi} \oint_c [A(\vec{r}) \frac{\partial v}{\partial n'} - v \frac{\partial A}{\partial n'}] \, ds \qquad (36)$$

where

$$v(\vec{r}_s, \vec{r}) = \ell n |\vec{r} - \vec{r}_s| - \ell n |\vec{r} - \frac{\vec{r}_s}{r_s^2}| - \ell n |\vec{r}_s| \quad ,$$

chosen such that $v(\vec{r}_s, \vec{r})$ vanishes for $|\vec{r}_s| = 1$. Again, the integral is a principal value integral at $\vec{r} = \vec{r}_s$.

Since $\psi = 0$ on the plasma vacuum boundary, we have, for r_s on the plasma surface

$$0 = -\frac{1}{2}(\vec{r}_s^{\,2} - 1) \frac{kB_z}{m} + \psi_w + \frac{1}{\pi} \oint_{p-v} [A(\vec{r}) \frac{\partial v}{\partial n'} - v \frac{\partial A(\vec{r})}{\partial n'}] \, ds \qquad (37)$$

and P -V indicates that the contribution to the integral arising from the integration along the wall vanishes since $A(\vec{r}) = 0$ and $v(\vec{r}_s, \vec{r}) = 0$ on the wall.

These equations are not appropriate for accurate numerical analysis because of the singular nature of the logarithmic potentials. Equation (35) is suitably modified by subtracting from each side, for fixed r_s , the constant function $\phi_s = \phi(r_s)$, which satisfies $\phi_s = \frac{1}{\pi} \int_c \phi_s \frac{\partial}{\partial n} \ell n |\vec{r} - \vec{r}_s| \, ds$, giving

$$0 = \frac{1}{\pi} \{[\phi(r) - \phi(r_s)] \frac{\partial}{\partial n} \ell n |\vec{r} - \vec{r}_s - \ell n |\vec{r} - \vec{r}_s \frac{\partial \phi(r)}{\partial n}\} \, ds \qquad (38)$$

Similarly, the function $A_s = A(r_s)$, constant in the plasma satisfies $A_s = -\frac{1}{\pi} \int_{p-r} A_s \frac{\partial v}{\partial n'}$, the sign change arising through $\hat{n}' = -\hat{n}$. Since $\psi = 0$ on the boundary, we have $A_s = \frac{1}{2}(r_s^2 - 1) - \psi_w$, and adding A_s to each side of Eq. (37) gives

$$0 = -(\vec{r}_s^{\,2} - 1)\frac{kB_z}{m} + 2\psi_w + \frac{1}{\pi} \int_{pv} \{[A(\vec{r}) - A(\vec{r}_s)] \frac{\partial v}{\partial n'} - v \frac{\partial A(r)}{\partial n'}\} \, ds \qquad (39)$$

The integrals in Eqs. (38) and (39) are then converted to finite sums over a discrete set of mass points and the resulting matrix equations for the values of $\partial\phi/\partial n$ and $\partial A/\partial n'$ on the plasma boundary are used to determine $\nabla\phi$ and $\nabla\psi$. These values are then used in Eq. (32) to step ϕ in time following the mass points, and $\nabla\phi$ is used to calculate the new position of the plasma boundary. An explicit two-step time stepping procedure was used, the values $\nabla\phi$, $\nabla\psi$ at time $t + \Delta t/2$ being used to step ϕ and the mass points from time t to time $t + \Delta t$. Typical time steps were $\Delta t = 5 \times 10^{-3}$, but Δt was continually adjusted to be compatible with the plasma velocity and mass point spacing. The initial selection of mass points cannot be maintained throughout the history of a run as the mass points tend to coalesce, and cease to provide a good representation of the plasma surface. They are, therefore, continually shifted on the surface through interpolation to provide roughly equal spacing.

Note added in proof: We have been informed that techniques and results similar to those in this section have also been achieved by Dnestrovskii, Zakharov, Kostomarov, Kukushkin, and Suzdaltseva.[5]

VI. CASE II; GENERAL CURRENT DISTRIBUTION

Given a general flux profile $\psi(r)$ in the plasma one has no choice but to use a two-dimensional grid in the plasma and finite difference Eqs. (15-21). We used a flux based coordinate system and a Lagrangian code, which makes the time advancement of ψ trivial. In addition, since the plasma vacuum boundary was a coordinate line, the usual numerical problems associated with a free boundary were alleviated.

Two approaches were used to construct the second coordinate. The first selected points so as to maintain a coordinate orthogonal to the ψ = constant lines, the second spaced the points equally along the ψ lines, and hence produced a non-orthogonal coordinate system.

The essential (time consuming) part of the numerical code in this case is the iterative solution to Poisson's equation which results from finite differencing Eq. (16) in time. To solve Poisson's equation ($\nabla^2 A = \rho$) for A with ($\partial A/\partial n$) known on an arbitrarily shaped boundary the following iteration scheme[6] is used,

$$\nabla^2_{AvE} A^{N+1} = \rho - (\nabla^2 A^N - \nabla^2_{AvE} A^N) \qquad (25)$$

where ∇^2_{AvE} is the Laplacian operator with the scale factors averaged around a ψ = constant surface (Fourier transforms

then being used on ∇^2_{AvE} . The convergence of this iteration procedure can be proved for orthogonal coordinates by using a variational principle, which also yields the rate of convergence. This is demonstrated in Appendix C. The non-orthogonal code will be discussed in a separate publication.

Aside from this interior relaxation problem, the solution is advanced in time in the same manner as described in Sec. V. Eq. (19) is solved to give $(\nabla_\perp \psi)^2_v$, and Eq. (18) used to advance $\frac{\partial A}{\partial n}$ in time. Once A is obtained in the plasma interior through the solution to the Poisson equation resulting from Eq. (16), it is in turn used to advance the positions of the mass points in time. Typically, time steps were $\Delta t = 0.005$, but the magnitude of the time step was continually adjusted to be compatible with the plasma velocity and the (changing) grid spacing.

A parabolic current $(J_z(r))$ profile vanishing on the surface and with no skin current $(\frac{\partial \psi}{\partial n}$ continuous and $q(0) = \frac{1}{2} q)$ was used for the first runs of this phase. In general, shear has a significant effect on the unstable modes. However, it has no effect on the $m = 1$ linear dispersion curve because the motion for $m = 1$ is just a solid displacement so that the plasma magnetic energy is not affected. In Fig. 9 is shown the growth rate for the case $\psi \equiv 0$ and the case of a parabolic profile.

As might be expected, shear also greatly effects the nonlinear development of the kink modes, even for an $m = 1$ perturbation. The results indicate that magnetic bubbles are not formed. However, the nonlinear distortions are still quite severe for $m = 1$. In Fig. 10a, b, c, and d, we present some typical final states, which are to be compared with the $\psi_p \equiv 0$ final states (Figs. 5, 6).

Probably more relevant to tokamaks are the $m = 2$ final states, examples of which we present in Fig. 11 e and f . These show that the nonlinear distortions are only moderate elongations of the plasma--with little or no concavity.

REFERENCES

[1] B. B. Kadomtsev and O. P. Pogutse, Proceedings of the Sixth European Conference on Controlled Fusion and Plasma Physics (Moscow, 1973), Sov. Phys.-JETP, 38 283, Zh. Eksp. Teor, Fiz. 65, p. 575 (1973).

[2] P. H. Rutherford, H. P. Furth, and M. N. Rosenbluth, in Plasma Physics and Controlled Nuclear Fusion Research (International Atomic Energy Agency, Vienna, 1971), Vol. 1, p. 533; presented at the Madison IAEA Conference (1971).

[3] V. D. Shafranov, Sov. Phys., Tech. Phys., 15, 175 (1970), Plasma Physics and the Problem of Controlled Thermonuclear Reactors (Pergamon, New York, 1958), Vol. IV.

[4] M. Chance, J. Greene, R. Grimm, J. Johnson (private communication).

[5] Y. N. Dnestrovski, L. E. Zakharov, D. P. Kostomorov, A. C. Kukushkin, L. F. Suzdaltseva, Pisma v, JTF (JTP Letters) 1 N1, p. 45 (1975).

[6] T. Oliphant (private communication).

[7] D. E. Potter and G. H. Tuttle, J. Computational Phys. 13, p. 483 (1973).

APPENDIX A

To derive Eq.(18), we dot Eq. (7) with $\hat{p}$, which yields

$$\rho \frac{D\vec{v}_\perp}{Dt} \cdot \hat{p} = -\frac{\hat{p} \cdot \nabla_\perp}{2} \{ (\nabla_\perp \psi)_v^2 - (\nabla_\perp \psi)_p^2 \} \qquad (A.1)$$

after using the pressure balance (Eq. [13]) and eliminating $B^2/2|_v$ by employing Eq. (12). Now,

$$\bar{v}_\perp \cdot \frac{D\hat{p}}{Dt} = ((v_\perp \cdot \hat{n})\hat{n} + (v_\perp \cdot \hat{p})\hat{p}) \cdot \frac{D\hat{p}}{Dt} = (v_\perp \cdot \hat{n})\hat{n} \cdot \frac{D\hat{p}}{Dt} \qquad (A.2)$$

and

$$\hat{n} \cdot \frac{D\hat{p}}{Dt} = \hat{n} \cdot \frac{D\vec{v}_\perp}{Ds} = \hat{n} \cdot (\hat{p} \cdot \nabla_\perp) \cdot \vec{v}_\perp \qquad (A.3)$$

where D/Ds is the derivative along the surface. Equation (18) now follows directly. (Equation [A.3] is most easily seen by using

$$\hat{p} = \frac{\bar{r}_{m+1} - \bar{r}_{m-1}}{|\bar{r}_{m+1} + r_{m-1}|}$$

where $\bar{r}_m$ is the position vector of the m^{th} surface point.)

APPENDIX B.

Zero resistivity implies a conserved integral of the motion, energy. This conservation can be derived directly from Eqs. (15-21), or from the usual conservation of

$\int_{plas} \{v^2 + \frac{B^2}{2}\} d\tau + \int_{vac} \frac{B^2}{2} d\tau$. However, it is easier to begin with Eq. (7) dotted with the velocity, from which we find the rate of change of the kinetic energy to be

$$\frac{d}{dt}\int \rho \frac{v^2}{2} d\tau = -\oint_{p-v} ds\,(\vec{n}\cdot\vec{v})\left[p + \frac{B^2}{2} - \frac{(\nabla\psi)^2}{2} + \frac{2kB_z}{m}\psi + \left(\frac{kB_z}{m}\right)^2 \frac{r^2}{2}\right] \qquad (B.1)$$

$$- \int \vec{v}\cdot\vec{\nabla}\psi\ \nabla^2\psi\ d\tau$$

Now use $p + \frac{B^2}{2}\Big|_p = \frac{B^2}{2}\Big|_v$, $\frac{d\psi_p}{dt} = 0$ and

$\frac{B_v^2}{2} + \left(\frac{kB_z}{m}\right)^2 \frac{r^2}{2} = \frac{(\nabla\psi)^2}{2}$ + const. in the vacuum to find

$$\frac{d}{dt}\int \rho \frac{v^2}{2} d\tau = -\oint_{p-v} ds\,(\vec{n}\cdot\vec{v})\left\{\frac{(\nabla\psi_v)^2}{2} - \frac{(\nabla\psi_p)^2}{2}\right\} + \int \frac{\partial\psi}{\partial t}\nabla^2\psi d\tau \quad . \qquad (B.2)$$

But

$$\frac{d}{dt}\int \frac{(\nabla\psi_p)^2}{2} d\tau = \int \frac{\partial}{\partial t}\frac{(\nabla\psi_p)^2}{2} d\tau + \oint_{p-v} \frac{(\nabla\psi_p)^2}{2}\,\vec{v}\cdot\vec{n}\ ds$$

and $\int \frac{\partial}{\partial t}\frac{(\nabla\psi_p)^2}{2} d\tau = \oint_{p-v} \frac{\partial\psi_p}{\partial t}\,\vec{n}\cdot\vec{\nabla}\,\psi_p\ ds - \int \frac{\partial\psi}{\partial t}\nabla^2\psi d\tau$.

On the surface $\frac{\partial\psi_p}{\partial t} = -\vec{v}\cdot\vec{\nabla}\psi$ so

$$\oint_{p-v} \frac{\partial\psi_p}{\partial t}\vec{n}\cdot\nabla\psi_p\ ds = -\oint_{p-v} (v\cdot\nabla\psi_p)(\vec{n}\cdot\nabla\psi_p)\ ds$$

$$= -\oint_{p-v} (\vec{v}\cdot\vec{n})\ (\nabla\psi_p)^2\ ds$$

and thus

$$\frac{d}{dt}\int \frac{(\nabla\psi_p)^2 d\tau}{2} = -\int \frac{\partial\psi}{\partial t}\nabla^2\psi\ d\tau - \oint_{p-v} \frac{\vec{v}\cdot\vec{n}}{2}(\nabla\psi_p)^2\ ds \qquad (B.3)$$

and

$$\frac{d}{dt}\int \{\rho\frac{v^2}{2} + \frac{(\nabla\psi_p)^2}{2}\}\, d\tau = -\oint ds\ \vec{n}\cdot\vec{v}\ \frac{(\nabla\psi_v)^2}{2} \quad . \qquad (B.4)$$

To evaluate the right hand side of Eq. (B.4), note that

$$\frac{d}{dt}\int \frac{(\nabla\psi_v)^2}{2} d\tau = \int \frac{\partial}{\partial t}\frac{(\nabla\psi_v)^2}{2} d\tau - \int ds\ \vec{n}\cdot v\ \frac{(\nabla\psi_v)^2}{2}$$

and further $\int \frac{\partial}{\partial t} \frac{(\nabla\psi_v)^2}{2} \, d\tau = \int \nabla\psi_v \cdot \nabla \frac{\partial \psi_v}{\partial t} \, d\tau$

which can be expressed as

$\oint ds \; \psi_v (\nabla \frac{\partial \psi_v}{\partial t} \cdot \vec{n})$ since $\nabla^2 \psi_v$ = constant.

Using a harmonic expansion for the vacuum solution

$$\psi = b(t) \, \ell nr + \psi_w(t) + \sum_m \psi_m(t) \, (r^m - r^{-m}) \cos m\theta + \frac{A(r^2-1)}{2}$$

this integral can be evaluated as

$$\oint ds \; \psi_v (n \cdot \nabla) \frac{\partial \psi_v}{\partial t} = 2\pi \, \psi_w \frac{\partial b}{\partial t} \quad . \tag{B.6}$$

Two types of boundary conditions can be imagined:

I. Constant current $\frac{\partial b}{\partial t} = 0$, then

$$\int \{ \rho \frac{v^2}{2} + \frac{(\nabla\psi_p)^2}{2} - \frac{(\nabla\psi_v)^2}{2} \} \, d\tau = \text{constant} \tag{B.7}$$

II. ψ_w = constant , then

$$\int \{ \rho \frac{v^2}{2} + \frac{(\nabla\psi_p)^2}{2} - \frac{(\nabla\psi_v)^2}{2} \} \, d\tau + 2\pi\psi_w b = \text{constant}. \tag{B.9}$$

APPENDIX C

The equation to be solved $\nabla^2 A = \rho$ can be written

$$\frac{\partial}{\partial x_1} F_1 \frac{\partial A}{\partial x_1} + \frac{\partial}{\partial x_2} F_2 \frac{\partial A}{\partial x_2} = \rho' = h_1 h_2 \rho \tag{C.1}$$

where h_1 and h_2 give the metric for the (orthogonal) coordinate system and $F_1 = h_2/h_1$, $F_2 = h_1/h_2$. The coordinate x_1 refers to the grid dimension perpendicular to the ψ = constant surfaces, x_2 to that along these surfaces. Defining $F = \bar{F} + \Delta F$ with $\bar{F}$ a function of x_1 only, we introduce an iteration scheme for A through

$$\frac{\partial}{\partial x_1} \bar{F}_1 \frac{\partial A^{N+1}}{\partial x_1} + \frac{\partial}{\partial x_2} \bar{F}_2 \frac{\partial A^{N+1}}{\partial x_2} = \rho' - \frac{\partial}{\partial x_1} \Delta F_1 \frac{\partial A^N}{\partial x_1} - \frac{\partial}{\partial x_2} \Delta F_2 \frac{\partial A^N}{\partial x_2} \; . \tag{C.2}$$

Given A^N , this equation may be inverted using Fourier transforms to find A^{N+1} . Let $A = A_0 + B$ with A_0 a solution to Eq. (C.1), and B satisfying the boundary condition $\partial B/\partial x_n = 0$. The iteration procedure for B is then

$$\frac{\partial}{\partial x_1} \bar{F}_1 \frac{\partial B^{N+1}}{\partial x_1} + \frac{\partial}{\partial x_2} \bar{F}_2 \frac{\partial B^{N+1}}{\partial x_2} = - \frac{\partial}{\partial x_1} \Delta F_1 \frac{\partial B^N}{\partial x_1} - \frac{\partial}{\partial x_2} \Delta F_2 \frac{\partial B^N}{\partial x_2} \; . \tag{C.3}$$

Consider the eigenvalue equation

$$\lambda_n \left[\frac{\partial}{\partial x_1}\bar{F}_1\frac{\partial B_n}{\partial x_1} + \frac{\partial}{\partial x_2}\bar{F}_2\frac{\partial B_n}{\partial x_2}\right] = -\left[\frac{\partial}{\partial x_1}\Delta F_1\frac{\partial B_n}{\partial x_1} + \frac{\partial}{\partial x_2}\Delta F_2\frac{\partial B_n}{\partial x_2}\right] \quad (C.4)$$

The eigenvalues follow from a variational principle

$$\lambda_n = \frac{-\int\left[\Delta F_1\left(\frac{\partial B^N}{\partial x_1}\right)^2 + \Delta F_2\left(\frac{\partial B^N}{\partial x_2}\right)^2\right]dx_1\,dx_2}{\int\left[\bar{F}_1\left(\frac{\partial B^N}{\partial x_1}\right)^2 + \bar{F}_2\left(\frac{\partial B^N}{\partial x_2}\right)^2\right]dx_1\,dx_2} \quad (C.5)$$

and $\lambda_n \le \max\left|\frac{\Delta F_1}{\bar{F}_1}\right|, \left|\frac{\Delta F_2}{\bar{F}_2}\right|$.

Moreover, the B_n corresponding to different λ_n are orthogonal. Hence, consider the quadratic form

$$I^N = \int\left[F_1\left(\frac{\partial B^N}{\partial x_1}\right)^2 + F_2\left(\frac{\partial B^N}{\partial x_2}\right)^2\right]dx_1\,dx_2$$

and normalize the B_n , solutions of Eq. (C.4) such that $I(B_n) = 1$. Then, if $B^N = \sum a_n^N B_n$, $I^N = \sum_n (a_n^N)^2$. From Eqs. (C.3) and (C.4)

$$B^{N+1} = \sum \lambda_n a_n^N B_n \quad (C.6)$$

and thus

$$\frac{I^{N+1}}{I^N} = \frac{\sum (a_n^N)^2 \lambda_n^2}{\sum (a_n^N)^2}$$ and

the quadratic form continually decreases if $\lambda_n < 1$.

Thus, to guarantee convergence, we must have $\left|\frac{\Delta F_{1,2}}{\bar{F}_{1,2}}\right| < 1$.

The optimum is to choose $\bar{F}_1$, $\bar{F}_2$ to be half the sum of maximum and maximum values along the ψ surfaces. The least convergent modes will presumably be those localized in a region where $\Delta F/\bar{F}$ is the largest, i.e., short wavelength. To maintain an orthogonal grid it was found sufficient to slide mass points along the ψ = constant surfaces after each time step, using local values of the normals to these surfaces to reconstruct an orthogonal grid after moving the grid points each time step, rather than use an integral method such as that developed by Potter.[7] The grid points were adjusted to be equally spaced either on the extreme inner, extreme outer, or central ψ surface. The disadvantage of this method is that moderate distortions of the plasma produce bunching of the grid points on other ψ surfaces (see Fig. 10). This

also increases the quantities ΔF_i , and leads to a less rapid convergence of the Poisson solver. Distortions somewhat greater than those shown in Fig. 10 were, in fact, impossible to follow.

Linear growth and oscillation rates produced by the code agree to within a few percent with analytic theory or (in the $m = 2$ case) radial numerical quadrature. An analytic nonlinear theory is being developed at this time to check the code in the region near the right hand marginal stable point ($q \neq$ integer). Other checks on the code are energy and area, which are conserved to within a few percent--even during the most severe nonlinear distortions.

FIGURE CAPTIONS

FIG. 1. The equilibrium plasma configuration

FIG. 2. Linear kink modes. The square of the growth rate is plotted versus nq/m for $m = 1, 2, 3$. The shaded region shows the range of q for which the bubble state is energetically favored. ($a = 0.5$.)

FIG. 3. Bubble state energy as a function of the plasma outer radius r_1 , $a = 0.5$.

FIG. 4. The undamped time history of the plasma surface in a case for which the bubble state is highly favored. Here $a = 0.7$, $\psi_w = -0.08$, $nq/m = 1.0$.

FIG. 5. Minimal Energy states, $a = 0.8$. Note that $\frac{\partial \psi}{\partial n}$ is discontinuous for $\psi_w < 0$.

FIG. 6. Minimal Energy states, $a = 0.5$.

FIG. 7. Minimal Energy states, $a = 0.7$, for (a) $m = 2$ and (b) $m = 3$. Here $\psi_w = -0.08$, $nq/m = 1.0$.

FIG. 8. Integration contours to determine (a) the velocity potential ϕ and (b) the flux function ψ .

FIG. 9. The effect of shear on the linear modes. The square of the growth rate is shown versus nq/m for $\psi \equiv 0$ and for a parabolic current profile $m = 2$.

FIG. 10. Minmal Energy states for $m = 1$ in the case of a parabolic current profile. Compare with Fig. 5.

FIG. 11. Minimal Energy states for $m = 2$ in the case of a parabolic current profile.

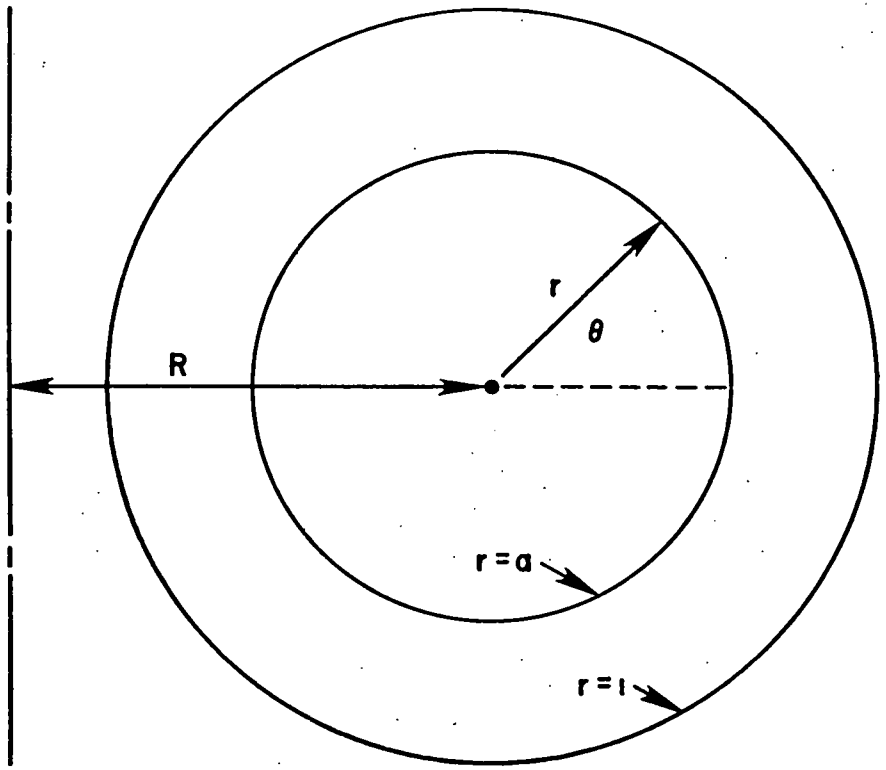

FIGURE 1

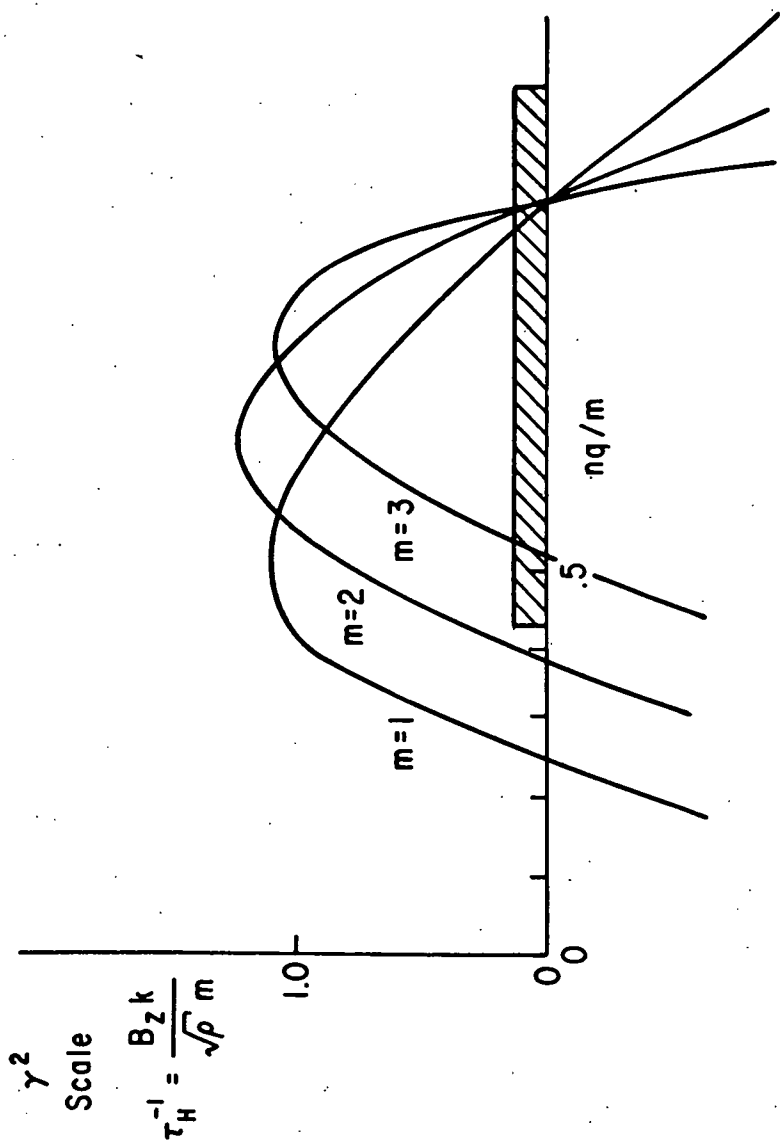

FIGURE 2

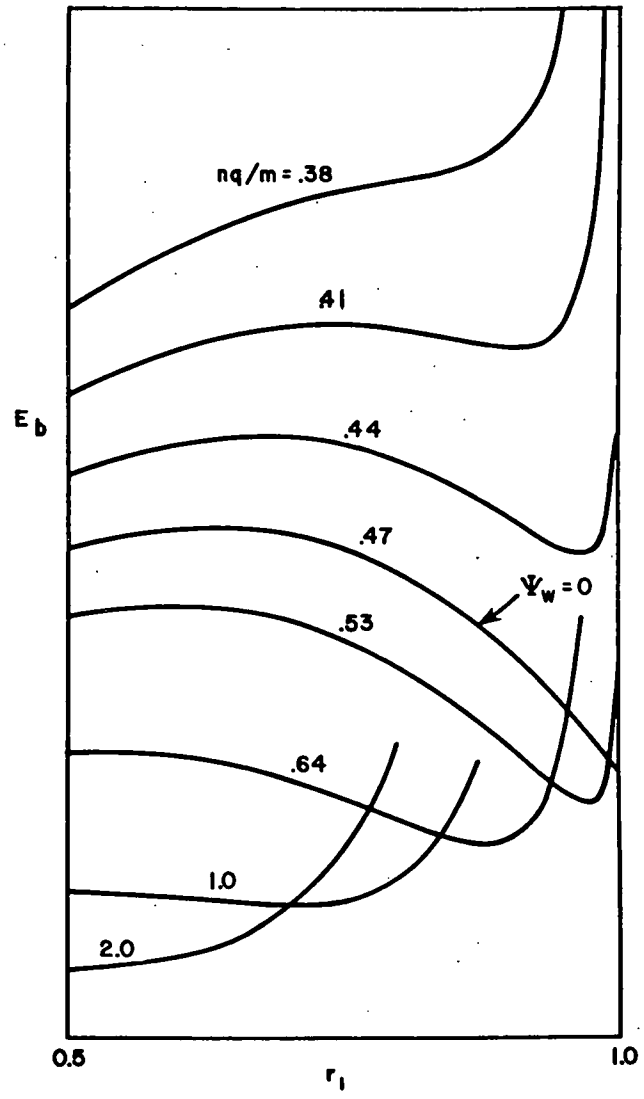

FIGURE 3

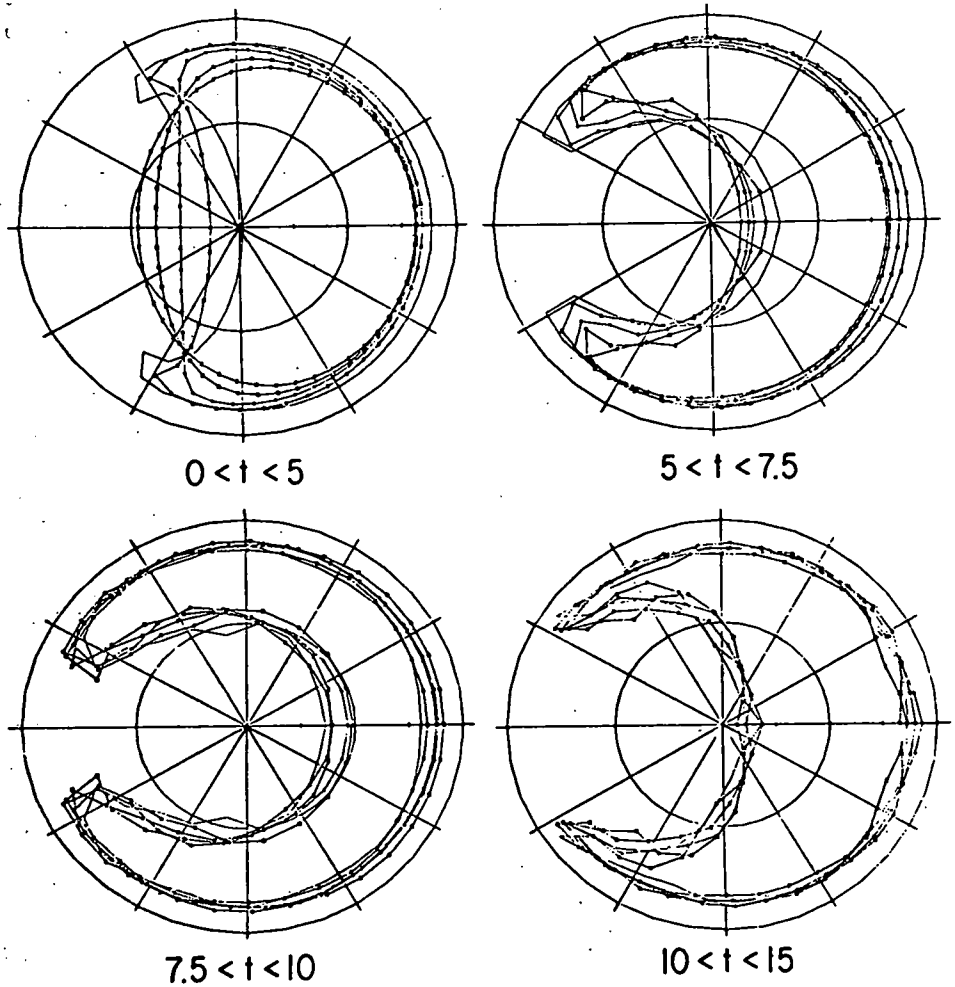

FIGURE 4

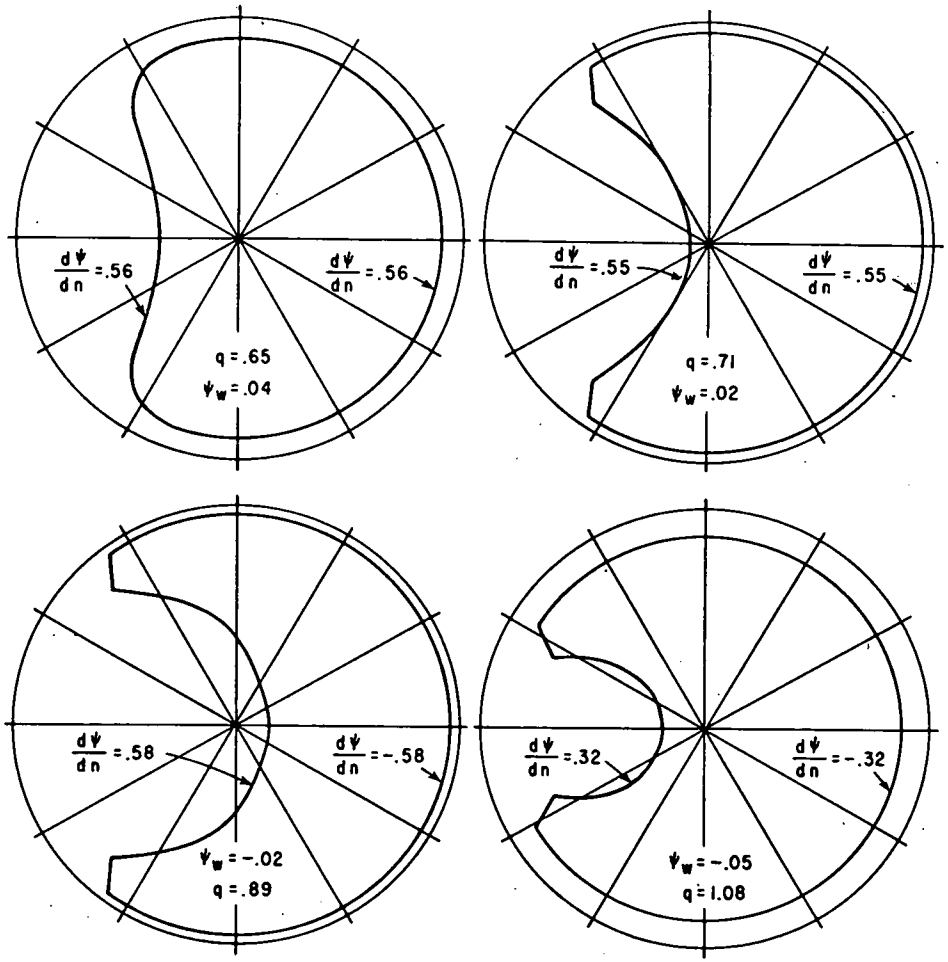

FIGURE 5

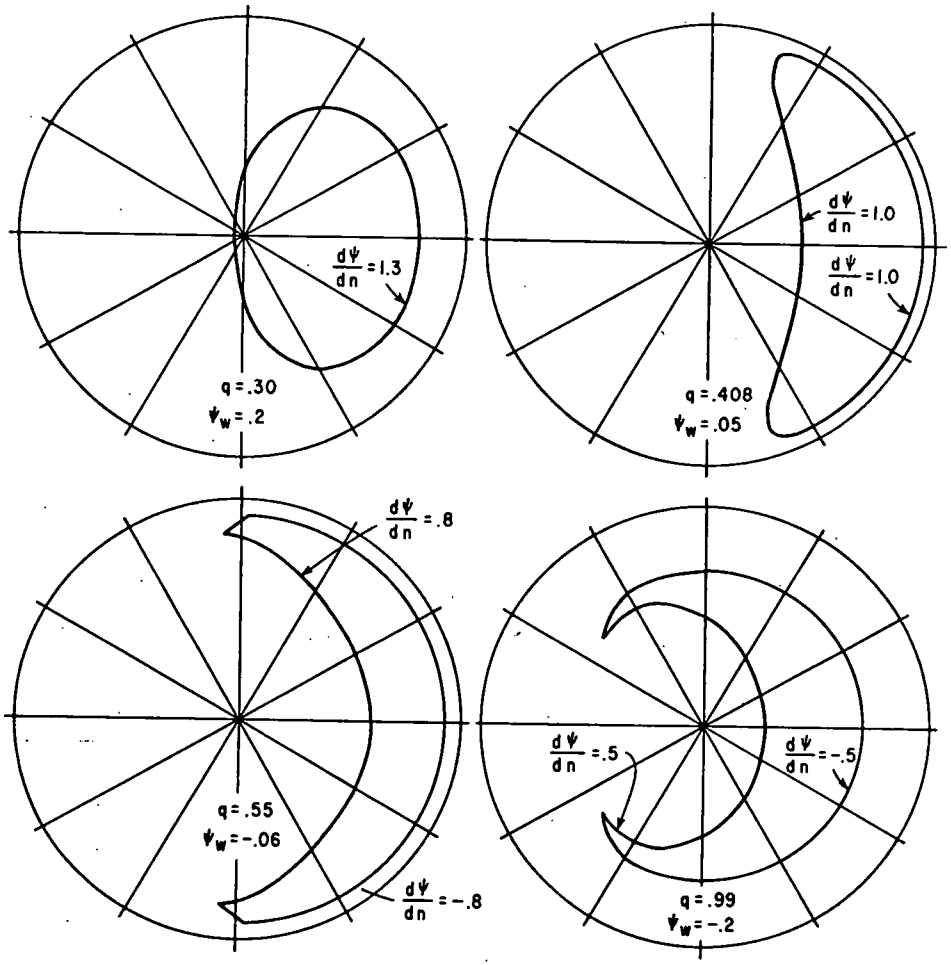

FIGURE 6

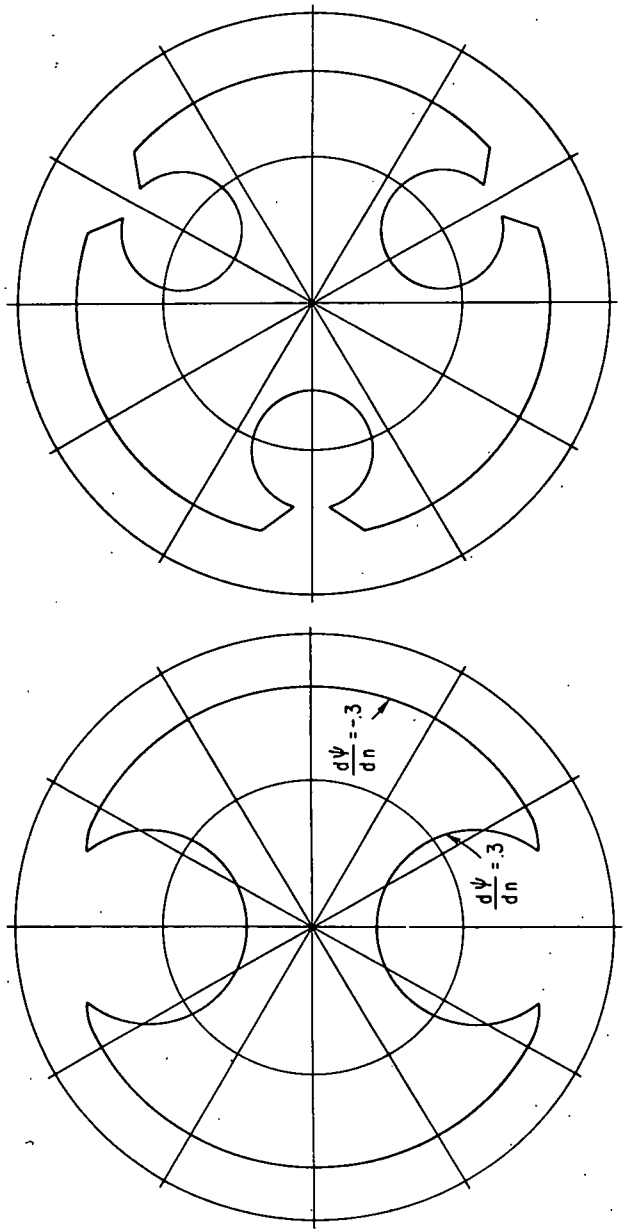

FIGURE 7

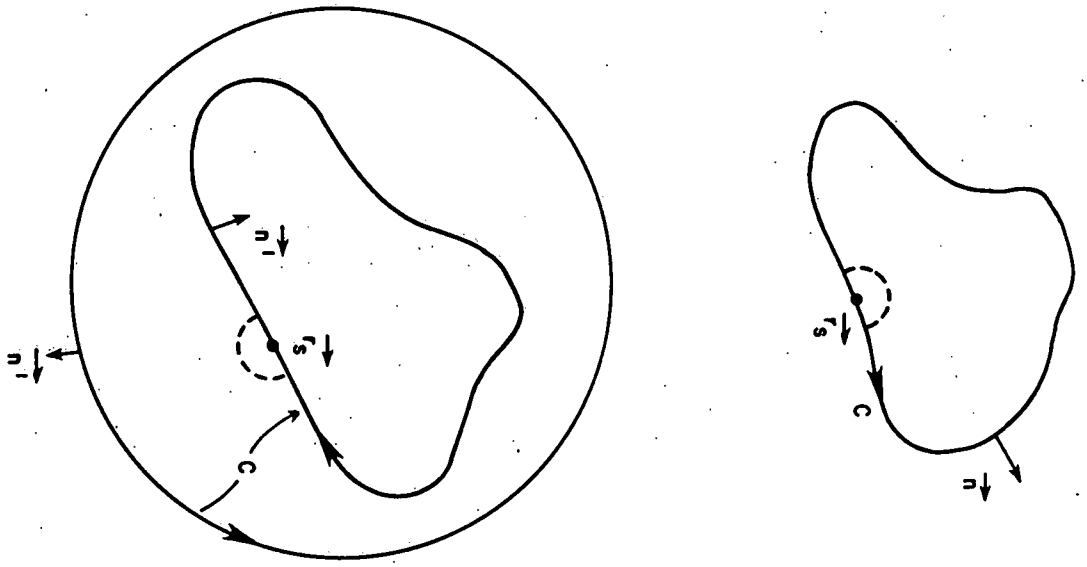

FIGURE 8

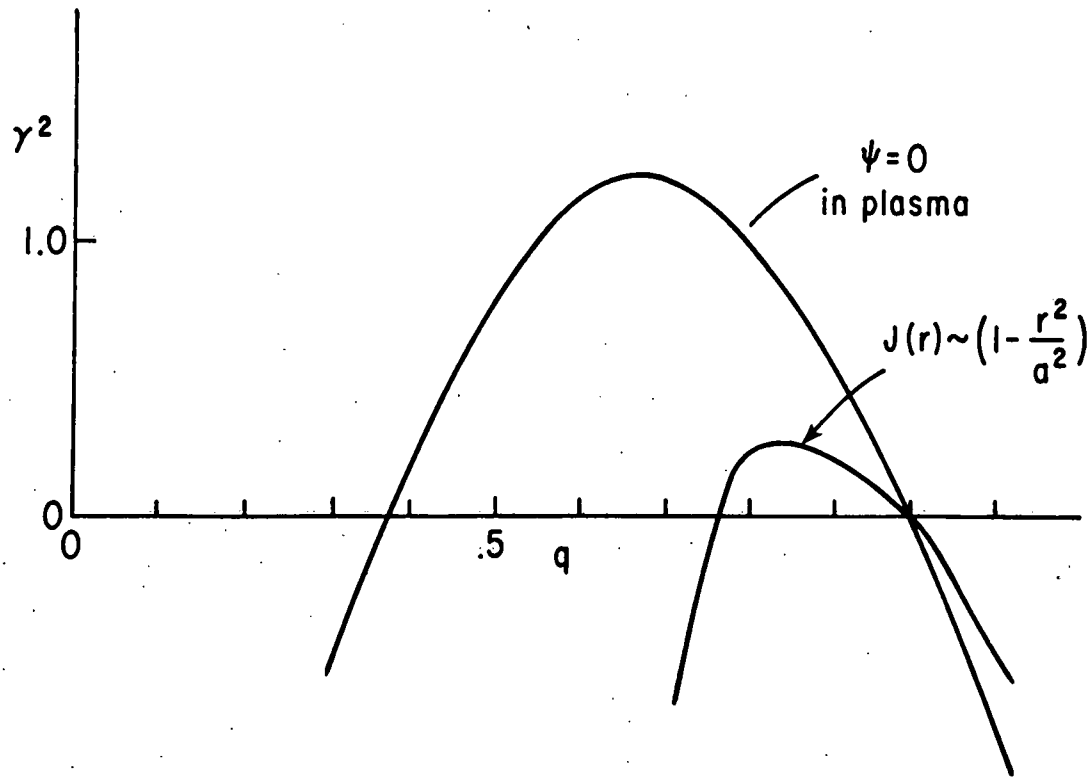

FIGURE 9

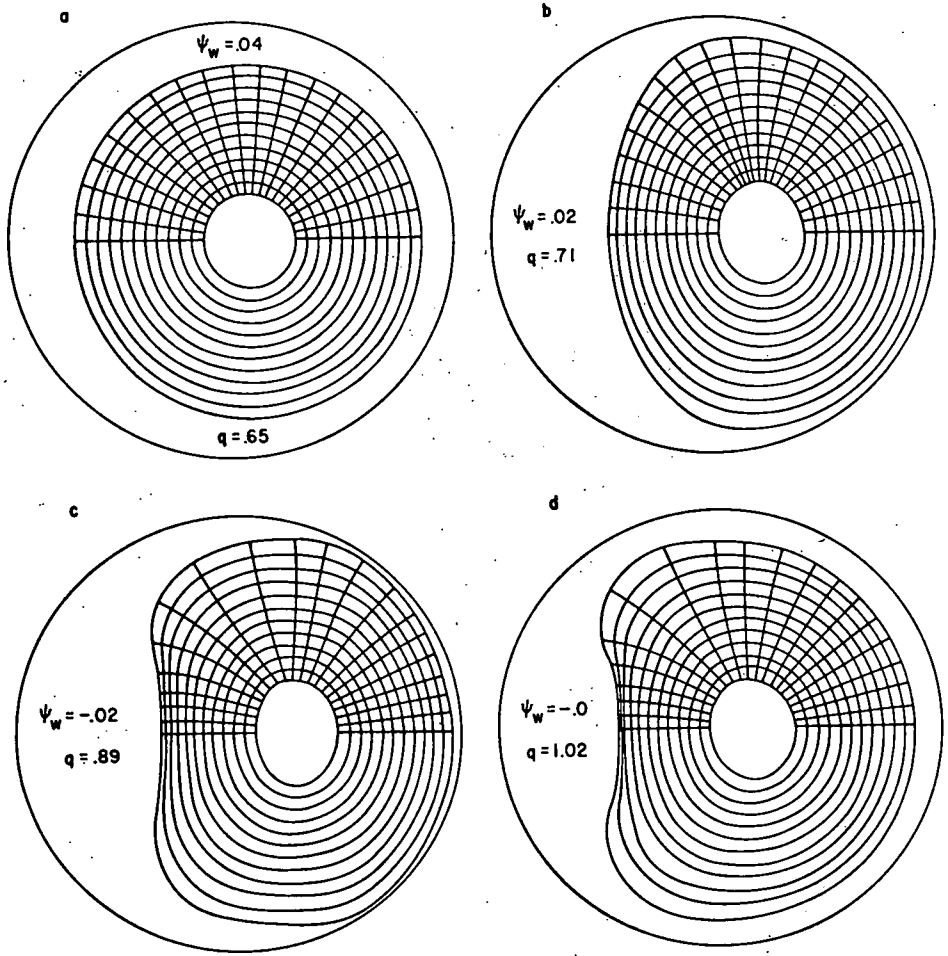

FIGURE 10

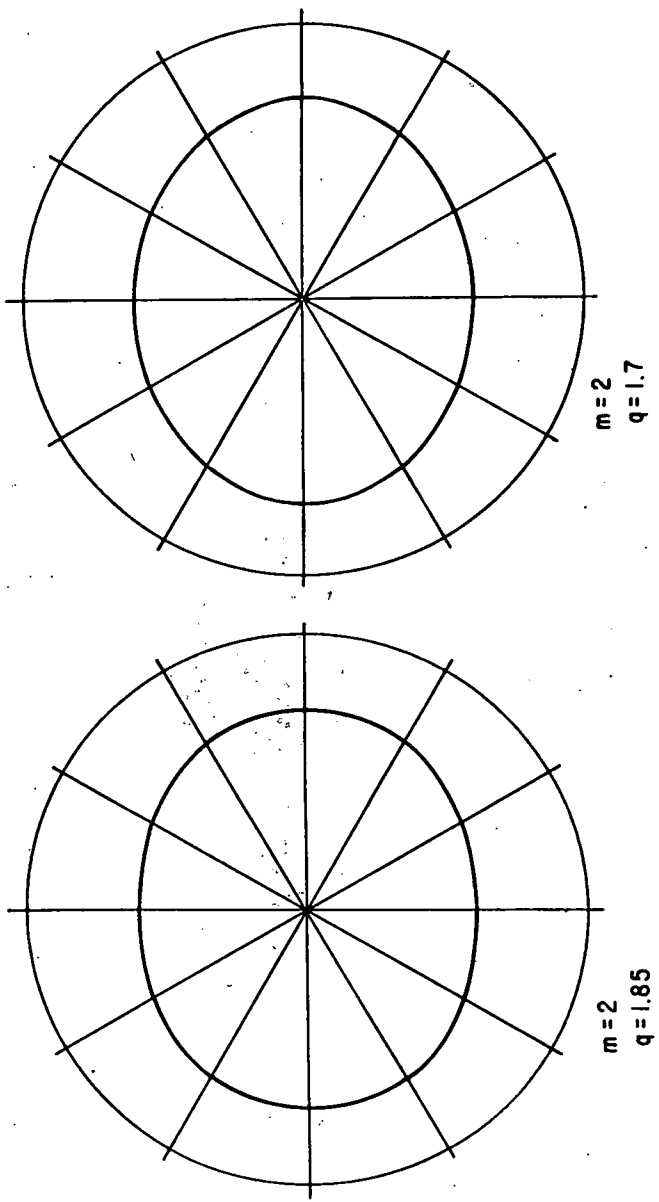

FIGURE 11